ORIGINAL ARTICLE

lajss.org© Latin American Journal of Solids and Structures

www.lajss.org

Failure response of expanded metal meshes subject to transversal impact

Gabriela Martínez[a], Euro Casanova[b], Carlos Graciano[c]*

[a]Universidad Austral de Chile, Facultad de Ingeniería, Instituto de Diseño y Métodos Industriales, Campus Miraflores, Valdivia, Chile.
Email: gabriela.martinez@uach.cl
[b]Universidad del Bío-Bío, Departamento Ingeniería Civil y Ambiental, Avenida Collao 1202, Concepción, Código Postal 4051381, Chile.
Email: ecasanova@ubiobio.cl
[c]Universidad Nacional de Colombia, Facultad de Minas, Sede Medellín, Departamento de Ingeniería Civil, A.A. 75267, Medellín, Colombia.
Email: cagracianog@unal.edu.co

* Corresponding author

https://doi.org/10.1590/1679-78257585

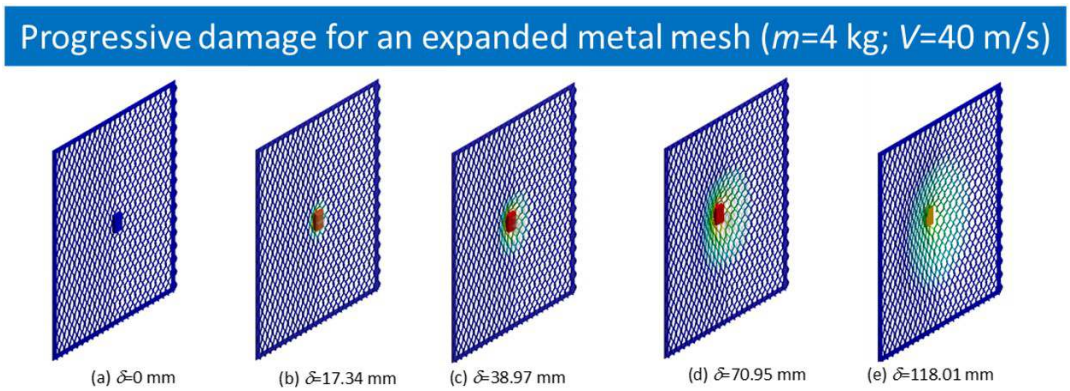
Abstract

This paper aims at investigating the failure response of expanded metal meshes subject to transversal impact. Firstly, the study is performed through explicit nonlinear finite element analysis, in which a numerical model is developed to determine the impact performance and failure mode of expanded metal meshes. Thereafter, the effect of expanded metal cell geometries, impact mass and velocity on the structural response of the meshes is analyzed. Then the perforation resistance of the impacted meshes is assessed and analyzed by means of vulnerability curves for various expanded metal geometries subject to transversal impact. The extent of damage in the meshes is also evaluated, and the maximum displacements achieved in each impact scenario is quantified. At the end, it is demonstrated that the perforation performance of the meshes depends on the expanded metal cell dimensions expressed as a combination of the strand cross-section and major axis length. Finally, the results also show the feasibility of using expanded metal meshes to protect structures impacted by flying debris.

Keywords

expanded metal mesh, flying debris, impact, perforation resistance, vulnerability curves, finite element analysis protective structures.

Graphical Abstract



Received March 18, 2023. In revised form March 24, 2023. Accepted June 14, 2023. Available online June 21, 2023.
https://doi.org/10.1590/1679-78257585

Latin American Journal of Solids and Structures. ISSN 1679-7825. Copyright © 2023. This is an Open Access article distributed under the terms of the Creative Commons Attribution License, which permits unrestricted use, distribution, and reproduction in any medium, provided the original work is properly cited.

1 INTRODUCTION

Climate change around the world has intensified weather effects on buildings and structures, particularly in those situations arising from wind events such as cyclones, tornados, hurricanes, and typhoons. Flying debris, in a strong wind environment, impacting on infrastructure cause damage in building envelopes including walls, roofs, doors, window shutters or screens, etc. (Minor, 1994). Additionally, in times of social unrest building envelopes require protection against possible violent acts during demonstrations. In this case, different objects may be thrown against structures causing significant material loses.

From a structural point of view, the use of elements in buildings as protective structures against impact of objects has been widely studied. Minor (1994) highlighted the importance of documenting the damage experience caused by storms and tornadoes to illustrate the significance of protecting a building envelope. Evaluation criteria to qualify products for use in building envelopes were described, and the evolution of these test standards and building codes criteria were followed. In many cases structural damage is unavoidable, nevertheless the damage can be mitigated by adequately accessing the corresponding protective system. In this sense, the response to windborne debris impact scenarios of various materials such as metal panels (Herbin and Barbato, 2012; Chen et al., 2014; Pathirana et al., 2017), expanded metal meshes EMM (Rambo-Roddenberry et al., 2012), structural insulated panels SIP (Chen and Hao, 2014; Meng et al., 2016; Chen et al., 2017; Saini and Shafei, 2020), cross-laminated timber CLT (Stoner and Pang, 2019), and wire meshes (Chen et al., 2017; Wang et al., 2021; Wang et al., 2022) have been analyzed. In these studies, the protective systems were experimentally tested, or numerically investigated, using a variety of masses, locations and velocities leading to the elaboration of vulnerability curves in which the corresponding limits for some combinations of these variables were established.

In comparison to other materials (SIP, CLT and wire meshes), EMM are an economic and environmental friendly alternative for protective systems. EMM are manufactured using low-carbon steel in different sizes and shapes through an in-line expansion process without welds (EMMA 557-20, 2020). EMM have been employed as part of rock fall protection systems in roads and their efficiency have been proven (Hwang et al. 2005; Ji et al. 2010; Lee et al., 2011). In crashworthiness, EMM have also been used (Smith et al., 2021), the crushing behavior of expanded metal tubes under compressive loading has been widely investigated throughout experimental testing (Graciano et al., 2009; Smith et al., 2014a, Smith et al., 2014b; Smith et al. 2016) and using numerical simulations (Smith et al. 2014b; Nedoushan, 2020; Martínez et al., 2013). The impact response of expanded metal tubes under axial crushing has also been investigated (Nouri et al., 2014; Hatami and Nouri 2015; Borges et al., 2016; Jahromi and Hatami, 2017; Graciano et al., 2017; Hatami et al., 2017). In a search for feasible applications of EMM in structural components subject to transversal impact, Taghipoor et al. (Taghipoor and Noori, 2018; Taghipoor and Nouri, 2020; Taghipoor et al., 2020) conducted a series of studies on the performance of lattice-core sandwich panels under impact scenarios. Rambo-Roddenberry et al. (2012) carried out an experimental study on the resistance to windborne debris impact of EMM, the meshes exhibited two damage mechanisms in which the mesh was either deformed or broken (**Figure 1**).

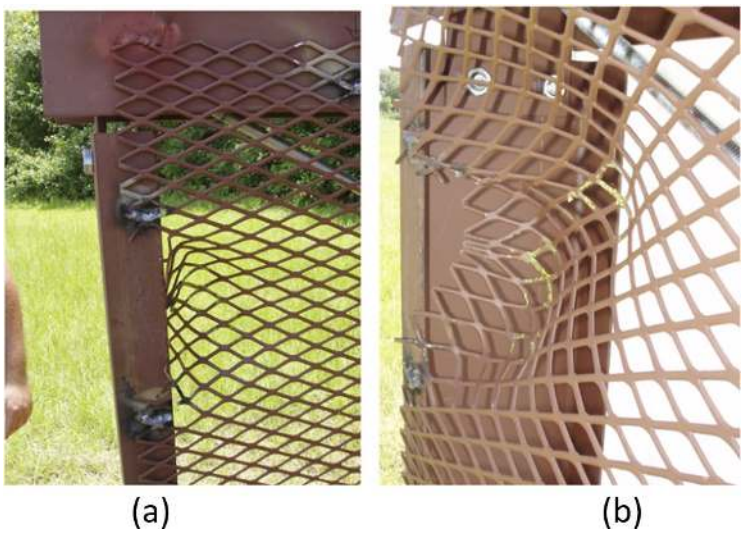


Figure 1: Residual deformation of EMM after missile impact: front view; (b) side view (Rambo-Roddenberry et al., 2012)

In recent years, there have been a growing use of expanded metal for aesthetic reasons and shading effects in façade claddings as shown in **Figure 2**, the mesh also works as a second skin to protect glass windows (Paule et al. 2006; Athens, 2007; Tsay et al. 2022; Khidmat et al. 2022; Rico-Martínez et al. 2022).



Figure 2: Expanded Metal Façade Cladding at Hyundai Motor Training Center, South Korea. https://www.metadecor.nl/projecten/hyundai-motor-training-center-in-zuid-korea/

As seen above, a proper estimation of the performance of EMM subject to transversal impact caused by flying debris is needed. Therefore, in this study the performance of EMM subjected to transversal impact is investigated. The study is conducted numerically using explicit nonlinear finite element analysis. Firstly, a numerical model is developed to study the impact response and failure modes of the meshes. Secondly, a parametric study is conducted to investigate the effect of impact masses and velocities, as well as mesh geometries on the impact performance of the mesh. The perforation resistance of the meshes impacted by flying debris was assessed performing a support-fail analysis, vulnerability curves and measuring the maximum displacements of the mesh. In the end, it is demonstrated that the perforation resistance of the meshes depends on the expanded metal cell dimensions, and a combination of the strand cross section and major axis length.

2 FINITE ELEMENT MODELLING

In this section, a numerical model of the EMM is elaborated using ANSYS Explicit Dynamics (ANSYS, 2020). In previous studies (Rambo-Roddenberry et al., 2012; Hwang et al., 2005; Ji et al., 2010; Lee et al., 2011), the response of EMM under transversal impact has been evaluated merely in qualitative terms, consequently the numerical procedure is verified herein considering the experimental study conducted by Chen et al. (2014) on corrugated steel panels impacted by flying debris. Thereafter, a parametric study is performed to analyze the effect of various variables on the impact response of the EMM. Moreover, the risk of failure of the meshes is also assessed by using vulnerability curves and evaluating their perforation resistance.

2.1 Numerical modelling for EMM

In **Figure 3**, the main features of an expanded metal cell are depicted, this cell can be defined using two orthogonal axes, a major axis l_1 and a minor axis l_2. Additionally, t and w represent correspondingly the strand thickness and width.

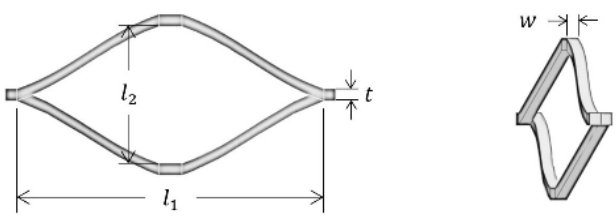


Figure 3: Notation for an expanded metal cell.

Similar to the corrugated panels tested by Chen et al. (2014), the dimensions of the EMM are 1200 mm by 762 mm. These dimensions are also comparable to those used by other authors (Herbin and Barbato, 2012; Meng et al., 2016; Saini and Shafei, 2020). As pointed out by Liu and Soares (2019), the resistance of plates strongly depends on the boundary conditions at the supports. In the numerical model, the expanded metal geometry is attached to a rigid frame with fixed supports at each of the contact points. This would be equivalent to supporting the mesh to the frame through weld points in each cell.

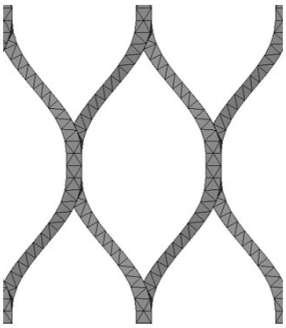


Figure 4: Finite element mesh for an expanded metal cell.

In the numerical model, the expanded metal mesh, the impact mass, and the rigid frame were modeled with SOLID 186 elements (ANSYS, 2020), which is suitable for plastic deformation studies. These elements were employed previously to study the quasi-static and dynamic response of expanded metal tubes under axial crushing (Graciano et al., 2012; Martínez et al., 2013; Smith et al., 2014b; Borges et al., 2016; Graciano et al., 2017). **Figure 4** shows a typical mesh of an individual cell.

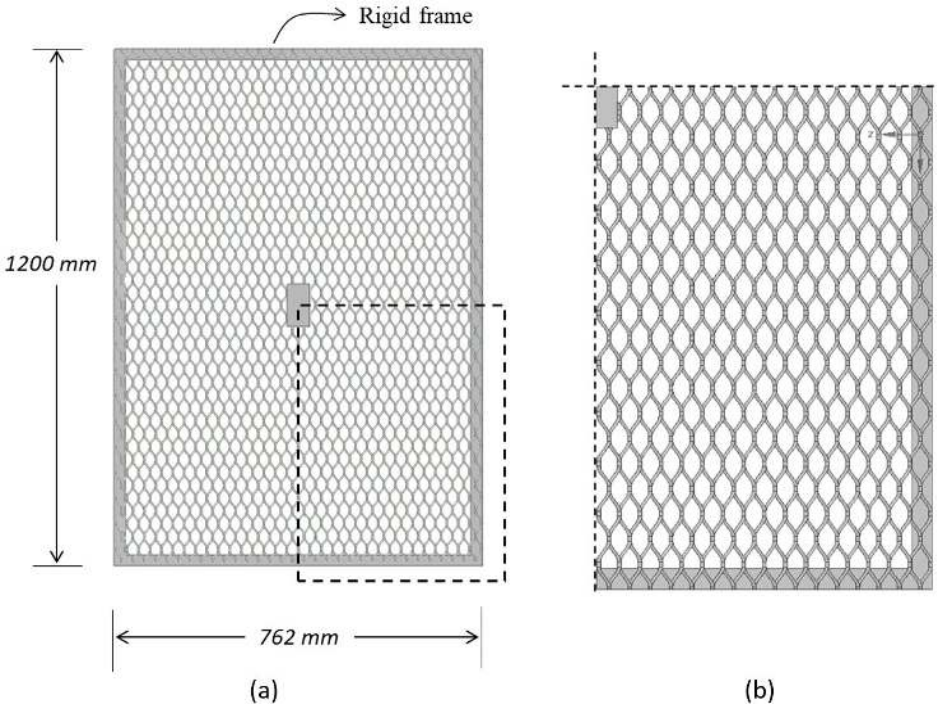


Figure 5: EMM geometry: (a) Dimensions and boundary conditions; (b) Axisymmetric model.

Figure 5a depicts the geometry of an expanded metal mesh and the supporting rigid frame. An impact mass of 100 mm x 50 mm is also illustrated in the middle of **Figure 5a**. It is clear that there is symmetry in geometry, loading protocol and support condition, therefore only a quarter of the total geometry is modeled. **Figure 5b** schematically shows the boundary conditions considered in the analysis. All degrees of freedom in the rigid frame are restricted to move in the impact direction. A bonded contact between the surfaces of the rigid support and the expanded metal mesh is defined.

The frame is modeled as a rigid solid while the debris is considered as a solid with an elastic modulus ten times higher than the EMM. The debris density is modified in order to change the magnitude of the masses. The debris is modelled employing a block geometry. The height of the debris was reduced, and the density modified proportionately to maintain its mass like in the verification procedure. The debris was given an initial velocity. The dimensions of the block are 100 mm x 50 mm (contact area) x 20 mm (height).

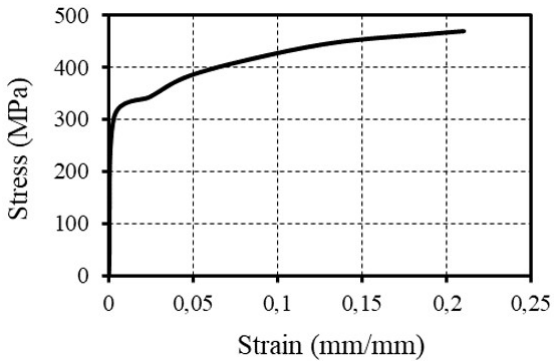


Figure 6: Stress-strain curve for expanded metal mesh.

EMM are mostly manufactured with ASTM A569 carbon steel, **Figure 6** shows the material characteristic curve employed in the numerical model. The Young's modulus is E= 205 GPa, and the Poisson's ratio is v= 0.3, quasi-static yield stress σ_s= 304 MPa, ultimate tensile stress σ_u= 470 MPa, fracture strain (mm/mm) ε_u=0.21. The Cowper-Symonds (1957) rate-sensitivity formulation was considered herein to account for dynamic loading effects

$$\frac{\sigma_d}{\sigma_s} = 1 + \left(\frac{\dot{\varepsilon}}{C}\right)^{\frac{1}{p}} \tag{1}$$

where σ_d is the dynamic flow stress at plastic strain rate, σ_s is the associated static flow stress, $\dot{\varepsilon}$ is the strain rate, the Cowper constant is C= 100 s^{-1}, and the Symonds constant is p = 10.

2.2 Modelling verification

In this section, the numerical procedure is verified using the results from the investigation performed by Chen et al. (2014) on the performance of corrugated panels impacted by windborne debris. Although the geometry of the panels is not similar to expanded metal mesh. It is important to reproduce Chen's model with the available numerical-computational tools. This verification makes it possible to establish a methodological pattern from a computational point of view based on current impact regulations. **Figure 7** depicts a view of the corrugated panels, in which the geometry corresponds to panels with industry standard size dimensions of 1200 mm by 762 mm, with a thickness of 0.42 mm. The height of the corrugation is 16 mm (**Figure 7**). These panels were modelled considering Zincalume AZ150 (grade G550 steel) with the following material properties: Young's modulus E= 220 GPa, Poisson ratio v= 0.3, quasi-static yield stress σ_s= 550 MPa, and density ρ= 7850 kg/m^3. The material is modeled using the kinematic hardening model proposed in Eq. (1). The erosion criterion of this material is defined using a failure strain of the plastic kinematic constitutive model, then, the failure (erosion) strain of the material was set to 0.17.

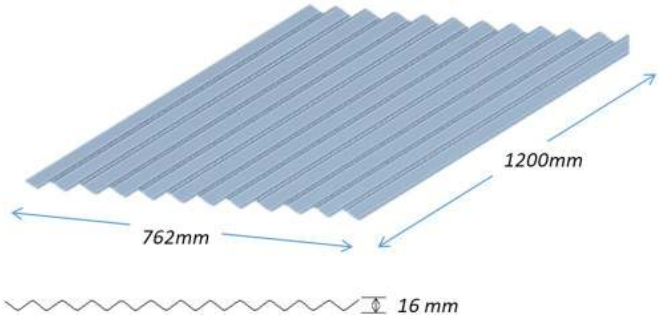


Figure 7: Numerical model of the corrugated steel panel tested by Chen et al. (2014).

This computational model was elaborated using ANSYS Explicit (ANSYS, 2020), following the description of the tests performed by Chen et al. (2014). Four-node quadrilateral shell elements (Shell163) were employed in this numerical model. Following the recommendations in various international standards (AS/NZS 1170.2:2021, 2021; ASTM E1996-20, 2020), during the tests, a wooden debris with a mass of 4 kg, with 900 mm in length, and cross-section of 100 mm by 50 mm was employed. The wooden debris impacted in the center of the panel at a velocity of 22 m/s. To simplify the numerical model, the height of the debris was reduced, and to maintain its mass the density increased proportionately (Mohotti et al., 2013). The boundary conditions were similar to those employed in the tests for specimen CP2 (Chen et al., 2014), in which the specimens were attached to a rigid frame with screws separated 20 cm along four edges. A convergence analysis was performed, the size of the elements was set at 2 mm, leading to a total mesh size with 71383 elements.

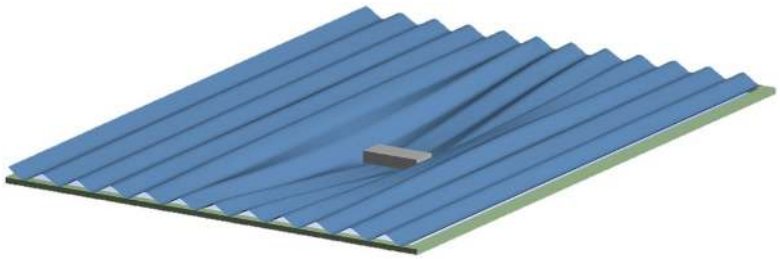


Figure 8: Numerical result for transversal impact of corrugated steel panel.

Figure 8 shows a deformation view of the corrugated panel after impact. A close agreement is observed between the displacement–time histories obtained experimentally by Chen et al. (2014) and obtained numerically in **Figure 9**.

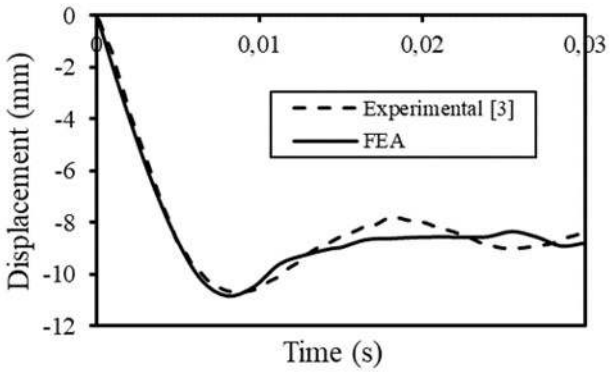


Figure 9: Comparison of displacement–time histories of CP2 supported condition.

2.3 Parametric study

To investigate the performance of EMM subject to transversal impact, two objective function are considered in this study: vulnerability which is the capacity of the EMM to withstand the impact, and deformability attained by determining the maximum deflection in the transverse direction. A sensitivity analysis is performed to investigate the effect of the following parameters on these objective functions:

- EMM cell geometry type: A, B and C
- Impact velocity: 15, 20, 25, 30, and 40 m/s
- Debris impact mass: 2, 4, 5, 6, and 8 kg

Table 1 shows the geometry of the three EMM Type A, B and C. Combining all these parameters yields to a total of 75 runs, 25 runs for each mesh type. The impact area of the debris, the overall size of the mesh, the support type and the materials properties remain constant through the whole parametric study.

Table 1: Geometry of various EMM cells used in the parametric study.

EMM Type	l_1 *(mm)*	l_2 *(mm)*	w (mm)	t (mm)	A_s (mm^2)	% open area	weight (kg/m^2)
A	76.2	33.8	5.2	5.0	26.0	69	12.37
B	50.8	23.4	3.8	3.4	12.9	68	9.10
C	61.0	25.1	6.1	4.3	26.2	52	17.36

Figure 10 presents a comparison of the size of the EMM used in the parametric study. As seen in Table 1, the cross-sectional area of EMM type A (A_s=26.0 mm^2) is similar to that of EMM type C (A_s=26.2 mm^2), and EMM type B has the smallest cross-section (A_s=12.9 mm^2).

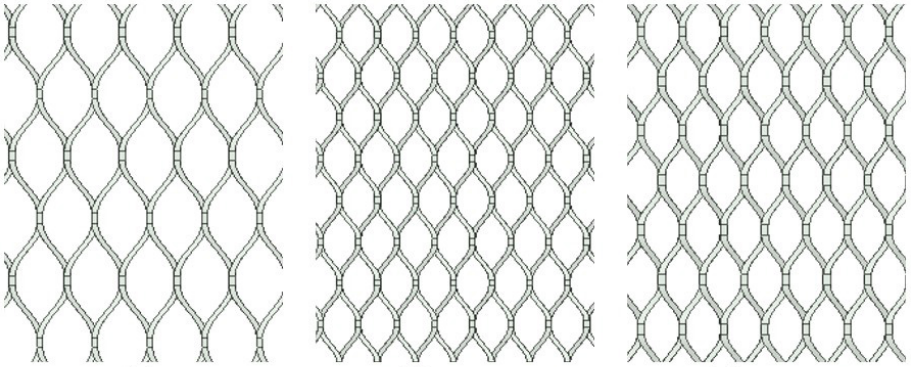


Figure 10: Comparative size of the EMM used in the parametric study.

3 RESULTS

In this section, the results are expressed in terms of vulnerability and displacement-time histories for all geometries, impact masses and velocities. In a previous stage, a convergence analysis is carried out to verify the sensitivity of the size of the elements on the impact response of the EMM.

3.1 Mesh convergence analysis

A convergence study was carried out for each type of mesh to be analyzed. All meshes type A, B and C were subjected to an impact mass of 4 kg with a velocity of 15 m/s for the convergence analysis. Thus, for mesh type A with w = 5.2 mm, element sizes of 6 mm, 5 mm, 4 mm, 3 and 2 mm were analyzed. **Table 2** shows the size of the meshes for each element size considering symmetry in geometry and boundary conditions, and also the maximum displacement δ_{max} computed accordingly.

Table 2: Results for the convergence analysis for EMM type A, m=4 kg, and V=15 m/s.

Element size (mm)	# Nodes	# Elements	δ_{max} (mm)
6	13238	25366	48.10
5	17195	38901	49.10
4	24465	65144	50.05
3	54641	154666	51.13
2	68793	220058	51.35

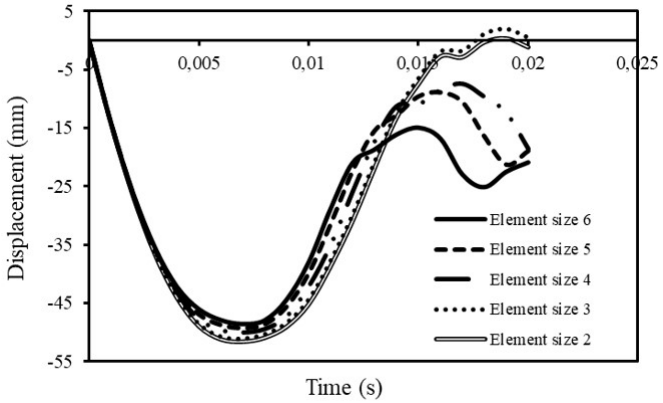


Figure 11: Convergence analysis for EMM type A (m=4kg, and V=15 m/s).

Figure 11 plots the maximum displacement in the case of EMM type A (*m*=4 kg and *V*=15 m/s). For EMM type A and type C with similar cross-sectional area (26.0 and 26.2 mm^2 respectively), an element size of 3 mm was selected. EMM type B has a smaller area (12.9 mm^2), therefore an element size of 2 mm was chosen.

3.2 *Vulnerability assessment*

In extreme situations, strong windstorms conditions and protests, debris of various sizes may fly at different velocities. Accordingly, a range of impact masses are considered herein beginning from 2.0 kg to 8.0 kg. Moreover, the range of velocities varies from 15 m/s to 40 m/s. These masses and velocities cover also the impact caused by intentionally thrown masses during demonstrations or acts where the integrity of facades can be affected.

Table 3 summarizes the results obtained numerically accessing the perforation performance of the analyzed EMM under various combinations of debris mass and velocity, where ‘‘P” indicates perforation of the mesh, and ‘‘N” non-perforation. For EMM type A, the panel withstand all debris impact masses at a velocity of 15 m/s, but fails when it is subjected to an 8 kg debris travelling at 20 m/s, the penetration resistance decreases with increasing velocity and mass. The panel is capable to reject an impact of a 2 kg debris at 40 m/s. For EMM type B and C, the penetration resistance decreases with respect to that of EMM type A. Both meshes failed to reject any debris mass impacting at a velocity of 40 m/s. Furthermore, these meshes were unable to withstand an impact mass of 8 kg, even travelling at the lower speed level *V*=15m/s.

Table 3: Perforation performance for EMM with respect to the debris mass and velocity.

EMM type	Mass (kg)	Velocity (m/s)				
		15	20	25	30	40
A	2	N	N	N	N	N
	4	N	N	N	N	P
	5	N	N	N	P	P
	6	N	N	P	P	P
	8	N	P	P	P	P
B	2	N	N	N	N	P
	4	N	N	P	P	P
	5	N	P	P	P	P
	6	N	P	P	P	P
	8	P	P	P	P	P
C	2	N	N	N	P	P
	4	N	N	P	P	P
	5	N	P	P	P	P
	6	N	P	P	P	P
	8	P	P	P	P	P

An alternative manner to visualize the results presented in **Table 3** is through the vulnerability curves plotted in **Figure 12**. Correspondingly, the EMM are capable to withstand the debris impact when the combination of mass and velocity is below the corresponding curve. For instance, EMM type A is capable to withstand a debris with *m*=3kg travelling at *V*= 30 m/s. In contrast, EMM type B and C are perforated for this combination of mass and velocity. For a debris with *m*=2kg and *V*=15 m/s, all EMM are capable to reject the debris, and hence protecting the structure. Based on the thresholds depicted in **Table 3** and **Figure 12** for the combination of debris mass and velocity to break the EMM, EMM type A achieved the best perforation performance. In contrast, EMM type C is more vulnerable to be perforated by the debris.

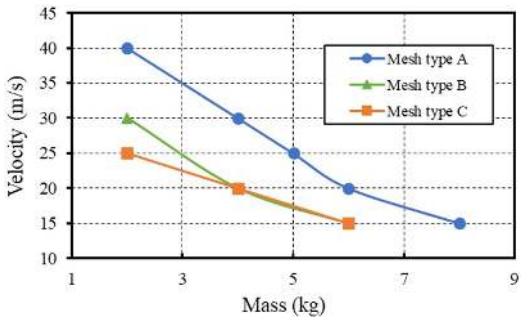


Figure 12: Vulnerability curves for EMM type A, B and C.

Figure 13a and **13b** plot the displacements and the corresponding von Mises stress distribution when a mesh type A is impacted by a debris with *m*=4 kg at *V*=15 m/s. Although the condition of symmetry in two planes of the part was used for the analysis, all the geometry is shown for better understanding. Clearly, the mesh is going to be permanently deformed as the achieved stress level exceeds the material yield strength σ_s= 304MPa. This effect is observed for all the analyzed meshes, except for EMM type B subjected to a mass *m*=4 kg at *V*=15 m/s, in which the maximum stress reached 287MPa (below yielding).

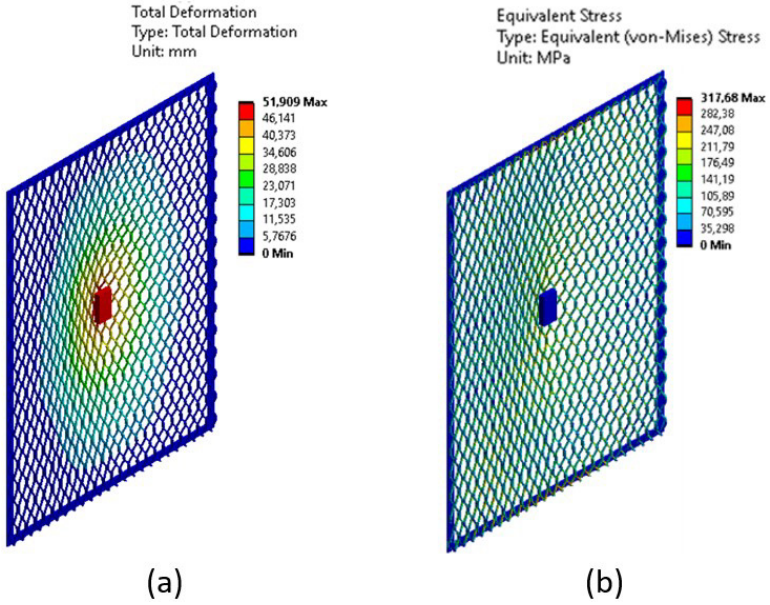


Figure 13: Numerical results for EMM type A, m=4kg, and V=15 m/s: (a) total displacements, (b) von Mises stress distribution.

Although the EMM provide an effective protection mechanism against debris impacts within the range of masses and velocities below the limits indicated in the vulnerability curves (**Figure 12**), these meshes are permanently deformed after the action of a debris, consequently, it is recommended to replace the EMM by others in original condition.

3.3 *Deformability assessment*

In the previous section, the performance of the meshes in terms of the perforation of the debris was qualitatively assessed. For practical purposes, it is also necessary to determine the maximum deflection, this will allow adjusting the design parameters and quantify the minimum safety distance between the mesh and the structures under analysis to fulfill the protection task. It should be noted that the surface area of the mesh to be evaluated, the impact surface and the mesh contour conditions remain constant during all simulations. **Figures 14**, **15** and **16** show the displacement-time histories for EMM type A, B and C, respectively. A comparison time of 30 ms was established for all simulations. This time allows to see the evolution of the maximum deformation, and in case of perforation, it is also evident in this interval.

Table 4: Maximum deflection δ_{max} (mm) for EMM type A, B and C.

EMM type	Mass (kg)	Velocity (m/s)				
		15	20	25	30	40
A	2	-34.94	-43.40	-51.67	-60.20	-77.65
	4	-51.91	-63.86	-76.64	-89.61	P
	5	-58.00	-72.30	-87.59	P	P
	6	-64.32	-80.06	P	P	P
	8	-74.70	P	P	P	P
B	2	-41.96	-52.01	-59.91	-69.98	P
	4	-63.86	-73.67	P	P	P
	5	-72.39	P	P	P	P
	6	-79.75	P	P	P	P
	8	P	P	P	P	P
C	2	-29.20	-36.82	-44.56	P	P
	4	-43.97	-54.75	P	P	P
	5	-50.37	P	P	P	P
	6	-55.14	P	P	P	P
	8	P	P	P	P	P

Table 4 shows the maximum deflection values reached in the meshes that were capable to reject the impact masses. EMM type B attained maximum deflection values for all velocities and masses, for a mass of 2 kg travelling at 15 m/s the maximum deflection is 41.96 mm, increasing the mass to 6 kg traveling at the same speed causes a maximum deflection of 79.75 mm.

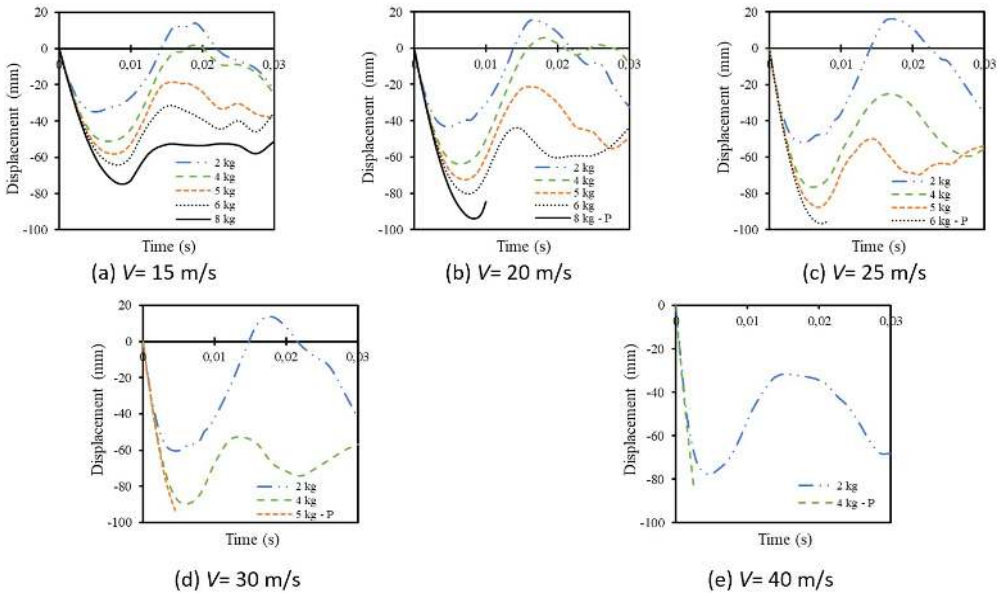


Figure 14: Displacement–time histories for EMM type A.

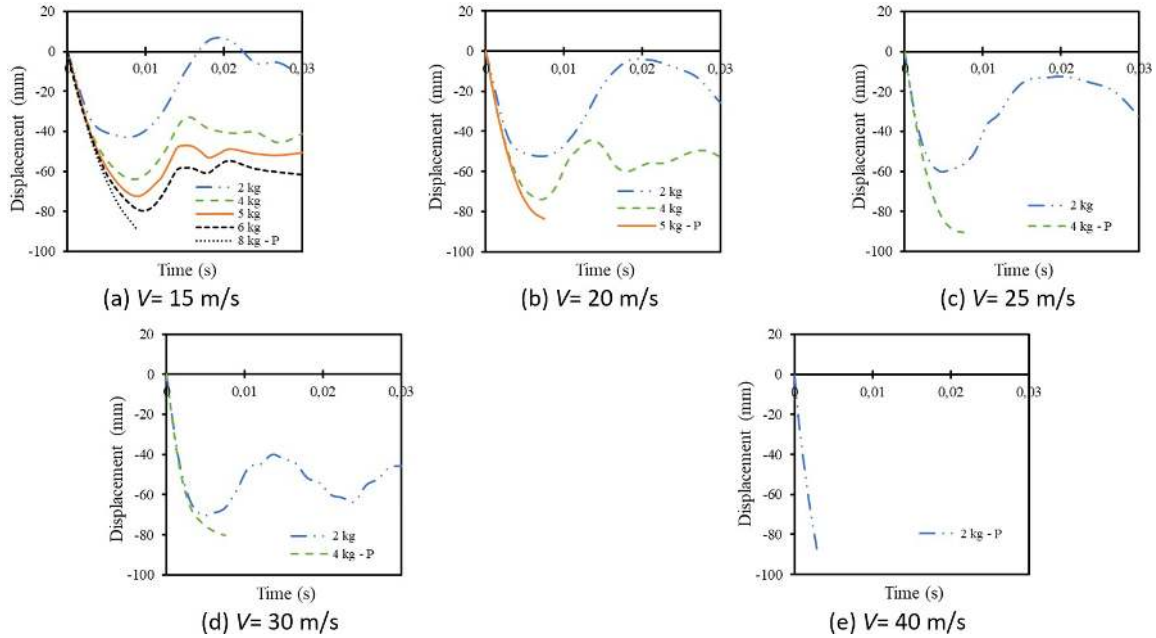


Figure 15: Displacement–time histories for EMM type B.

Figures 14, **15** and **16** show a behavior of increasing deformations as the velocity of the impacted mass increases. For all mesh types, once the maximum displacement is achieved the displacement-time histories exhibit rebounds. In some cases, especially at high velocities the meshes are unable to reject the impact masses, hence breakage of the meshes is reached. These velocity and mass limits in which the EMM are broken represented the thresholds previously shown in Table 3 and **Figure 12**.

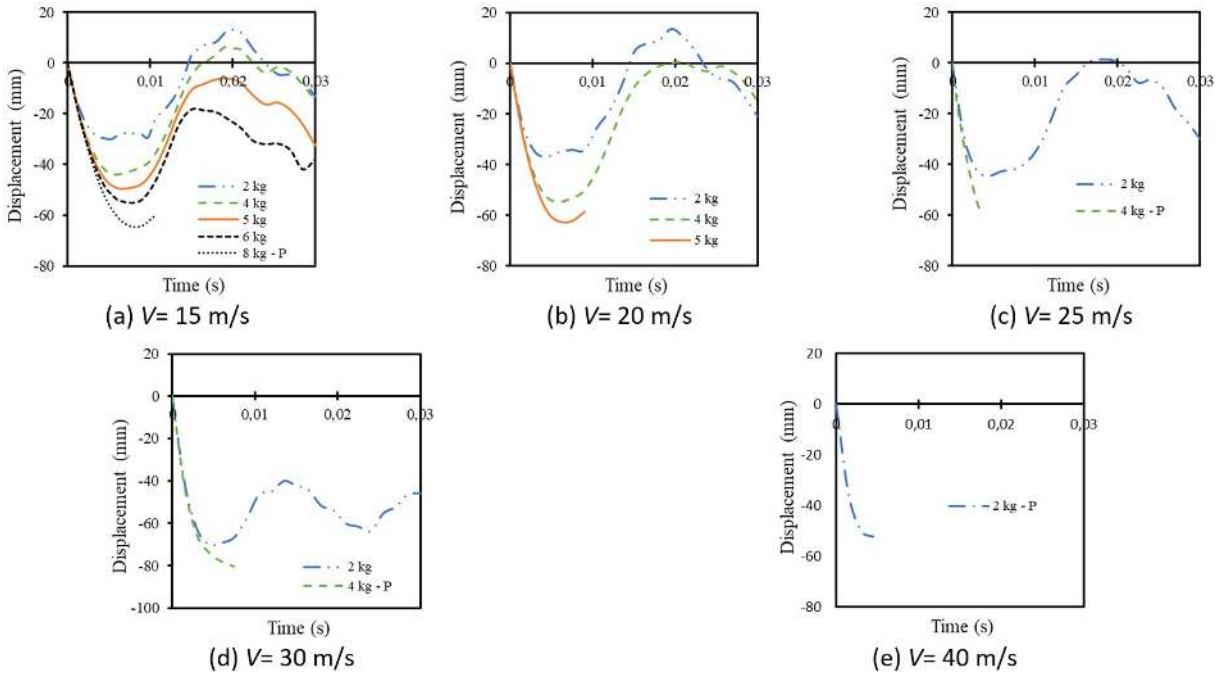


Figure 16: Displacement–time histories for EMM type C.

Figure 17 shows the relationship between the maximum displacements reported in Table 4 and the impact masses for the three EMM types at *V*=15 m/s. EMM type C attained the lowest displacements, while EMM type B attained the largest displacement. It is worth pointing out that the expanded metal cells for the three meshes are different, both the dimensions of the strand cross-sections and the opening sizes (given that the lengths of the major and minor axes in **Table 1**) are different.

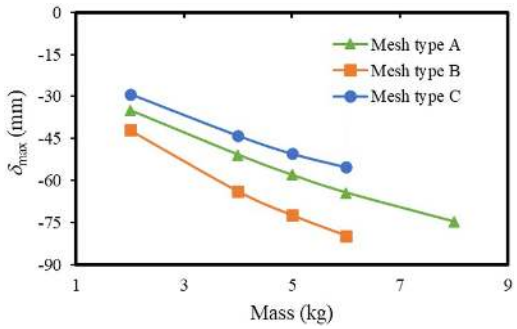


Figure 17: Relationship between impact mass and δ_{max} for all EMM at V=15 m/s.

3.4 Failure mechanism analysis

Figure 18 illustrates the progressive damage for mesh type A impacted by a mass of 4 kg at 40 m/s. As seen in **Figure 18b** to **Figure 18e**, the expanded metal cells in the central area of the panel, in the plane of the mesh and perpendicular to the impact load, undergo large displacements through a flexural mechanism in which the open area of the mesh significantly increases. At the same time, the stress levels also increase until the mesh is unable to withstand the impact, and hence the strands are strained to the point of breaking (**Figure 18e**).

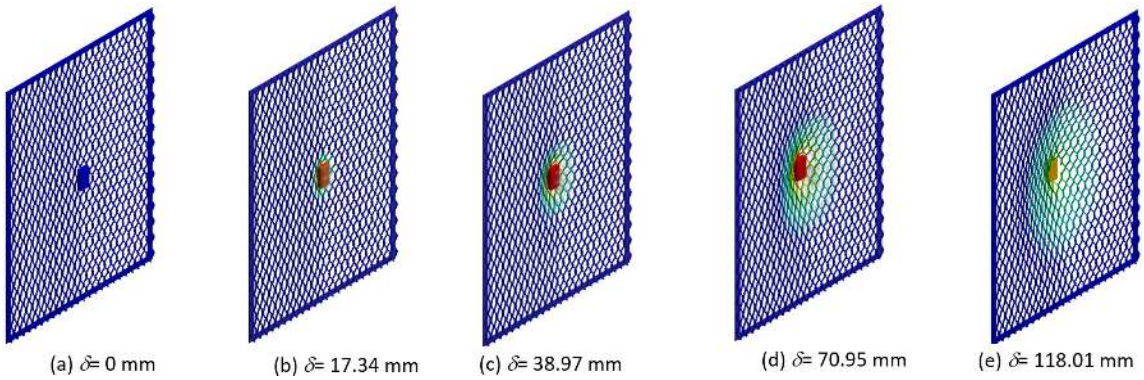


Figure 18: Progressive damage for EMM type A (m=4 kg; V=40 m/s).

In various studies regarding the collapse mechanism of EMM subject to compressive or shear loading (Graciano et al., 2009; Graciano et al. 2012; Martínez et al., 2013; Borges et al., 2016; Teixeira et al., 2016; Graciano et al., 2019), the expanded metal cell exhibits a bending mechanism in which the strands in the mesh undergo high levels of plastic deformation in the nodes (**Figure 19**).

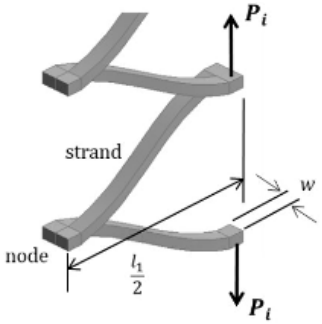


Figure 19: Free body diagram of a single EMM strand under bending.

Figure 19 shows the free body diagram of a single expanded metal strand under bending. According to Graciano et al. (2012), the load P_i required to attain the plastic moment capacity forming a plastic hinge in the node of an expanded metal cell is

$$P_i = 2\sigma_y \frac{wt^2}{l_1} \tag{2}$$

To obtain Eq. (2), it was assumed that each strand in an expanded metal mesh behaves like a beams subject to bending. From Eq. (2), it is also clear that the following parameter is representative of the flexural stiffness of an expanded metal cell

$$\theta = \frac{wt^2}{l_1} \tag{3}$$

This parameter was also employed to investigate the effect of the cell size on the impact response of expanded metal tubes (Borges et al., 2016; Graciano et al., 2017). **Figure 20** plots the maximum displacements attained for the EMM in terms of the flexural stiffness represented by ϑ and calculated with Eq. (3). It is clearly observed the maximum deflection varies with the cell stiffness, the larger the stiffness the smaller is the maximum deflection. For EMM type B (ϑ=0.86) impacted with a mass of 6 kg the maximum displacement is 79.75 mm. In contrast, for EMM type C (ϑ=1.85), when it is impacted with a mass of 6 kg the maximum displacement is 55.14 mm, and for EMM type A (ϑ=1.706) the maximum displacement is 64.32 mm. In summary, the largest the stiffness the lowest the maximum displacement.

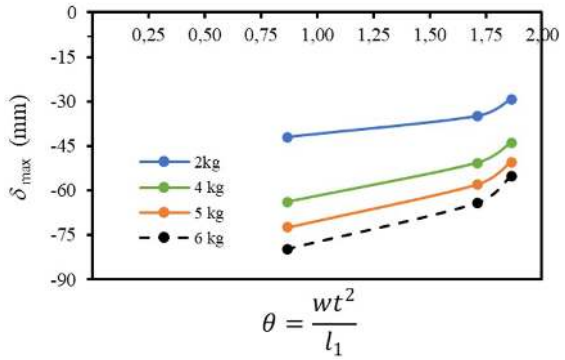


Figure 20: Maximum displacement in terms of the stiffness θ of the expanded metal cells (V=15m/s).

4 CONCLUSION

In this work, the failure response of EMM subjected to transversal impact caused by flying debris was investigated herein through explicit nonlinear finite element analysis. A numerical model was developed to simulate the mesh responses towards transversal debris impacts. The numerical methodology was verified by comparison with experimental results available in the literature. Afterwards, a parametric study was conducted considering various debris masses and velocities, as well as various expanded metal cell geometries.

Vulnerability curves of the meshes were elaborated in terms of the impact mass and velocity. From the results, both the impact mass and velocity affect the impact performance of the EMM. It was observed that the penetration resistance of the meshes depends on the expanded metal cell dimensions, a combination of the strand cross section and major axis length. It was demonstrated that EMM are capable to withstand flying debris impacts. EMM are a feasible alternative to protect structures subjected to debris impacts.

It is noteworthy that additional experimental tests are still required to further verify the penetration resistance of EMM. Some additional parameters should be included in future studies such as the stiffness of the supporting frame, impact location and the material properties of the mesh.

Author's Contribuitions: Conceptualization, G Martínez and C Graciano; Methodology, G Martínez, E Casanova and C Graciano; Investigation, G Martínez, E Casanova and C Graciano; Writing - original draft, G Martínez and C Graciano; Writing - review & editing, G Martínez, E Casanova and C Graciano; Resources, G Martínez, E Casanova and C Graciano; Supervision, C Graciano.

Editor: Marcílio Alves

References

ANSYS (2020), Inc. Products 2020 R1, Workbench User's Guide.

Athens, L. (2007). Design for Social Sustainability at Seattle's Central Library. Journal of Green Building, 2(1), 1-21. https://doi.org/10.3992/jgb.2.1.1.

Australian/New Zealand Standard (2021). AS/NZS 1170.2-2021 structural design actions Part 2: wind actions. Sydney, NSW: Australian/New Zealand Standard.

ASTM E1996-20 (2020). Standard Specification for Performance of Exterior Windows, Curtain Walls, Doors and Storm Shutters Impacted by Windborne Debris in Hurricanes. West Conshohocken, PA, USA: American Society for Testing and Materials.

Borges H., Martínez G., Graciano C., (2016). Impact response of expanded metal tubes: A numerical investigation, Thin-Walled Structures 105(1), 71–80. https://doi.org/10.1016/j.tws.2016.04.005.

Cowper G.R., Symonds P.S., (1957). Strain-Hardening and Strain-Rate Effects in the Impact Loading of Cantilever Beams. Brown University Division of Applied Mathematics, Providence, Rhode Island, USA.

Chen W., Hao H., (2014). Experimental and numerical study of composite lightweight structural insulated panel with expanded polystyrene core against windborne debris impacts. Materials and Desing 60, 409–423. https://doi.org/10.1016/j.matdes.2014.04.038.

Chen W., Hao H., Du H., (2014). Failure analysis of corrugated panel subjected to windborne debris impacts. Engineering Failure Analysis 44, 229–249. https://doi.org/10.1016/j.engfailanal.2014.05.017.

Chen W. S., Hao H., Meng Q. F., (2017). Experimental study of steel wire mesh reinforced structural insulated panels against windborne debris impact. In Mechanics of Structures and Materials: Advancements and Challenges - Proceedings of the 24th Australasian Conference on the Mechanics of Structures and Materials, ACMSM24 2016, 571–576.

EMMA 557-20 (2020): Standards for expanded metal. Expanded Metal Manufacturers Association (EMMA). Division of the National Association of Architectural Metal Manufacturers (NAAM).

Graciano C., Martínez G., Smith D., (2009). Experimental investigation on the axial collapse of expanded metal tubes. Thin-Walled Structures 47, 953–961. https://doi.org/10.1016/j.tws.2009.02.002.

Graciano C., Martínez G., Gutiérrez A., (2012). Failure mechanism of expanded metal tubes under axial crushing, Thin-Walled Structures, 51(1), 20–24. https://doi.org/10.1016/j.tws.2011.11.001.

Graciano, C., Borges, H., Martínez, G., Teixeira, P., (2017). Axial crushing of concentric expanded metal tubes under impact loading. Latin American Journal of Solids and Structures, 14, 874-885. https://doi.org/10.1590/1679-78253670.

Graciano C, Teixeira P, Martinez G., (2019). Yielding shear resistance of expanded metal panels. Thin-Walled Structures, 138:286–292. https://doi.org/10.1016/j.tws.2019.02.024.

Hatami, H. A., Nouri, M. D., (2015). Experimental and numerical investigation of lattice-walled cylindrical shell under low axial impact velocities. Latin American Journal of Solids and Structures, 12, 1950-1971. https://doi.org/10.1590/1679-78251919.

Hatami H., Shokri-Rad M., Ghodsbin-Jahromi M., (2017). A theoretical analysis of the energy absorption response of expanded metal tubes under impact loads. International Journal of Impact Engineering 109(1), 224–239. https://doi.org/10.1016/j.ijimpeng.2017.06.009

Herbin A.H., Barbato M., (2012). Fragility curves for building envelope components subject to windborne debris impact. Journal of Wind Engineering and Industrial Aerodynamics 107, 285–298. https://doi.org/10.1016/j.jweia.2012.05.005.

Hwang, Y. C., Kim, B. J., Noh, H. J., (2005). Development and performance evaluation of the expanded metal rockfall protection fence. Journal of the Korean Geo-Environmental Society, 6(3), 35–45.

Jahromi A.G., Hatami H., (2017). Energy absorption performance on multilayer expanded metal tubes under axial impact. Thin-Walled Structures 116(1), 1–11. https://doi.org/10.1016/j.tws.2017.03.005.

Ji, Y., Kim, K., Kim, S., Hwang, Y., Lee, S., (2010). A study on protection depending on mesh size of expanded metal for slope reinforcement. JournaL of the Korean Geo-Environmental Society, 11(12), 47–56. (In Korean).

Khidmat, R. P., Fukuda, H., Paramita, B., Qingsong, M., Hariyadi, A., (2022). Investigation into the daylight performance of expanded-metal shading through parametric design and multi-objective optimisation in Japan. Journal of Building Engineering, 51, 104241. https://doi.org/10.1016/j.jobe.2022.104241

Lee, J. I., Jung, C. G., Kim, S. H., Hwang, Y. C., Lee, S. H., (2011). A study on the evaluation of expanded metal characteristics for application rockfall facilities. JournaL of the Korean Geo-Environmental Society, 12(9), 13–20. (In Korean).

Liu, B., Soares, C.G., (2019). Effect of strain rate on dynamic responses of laterally impacted steel plates. Int.ernational Journal of Mechanical Sciences, 160, 307–317. https://doi.org/10.1016/j.ijmecsci.2019.06.034.

Martínez, G., Graciano, C., Teixeira, P., (2013). Energy absorption of axially crushed expanded metal tubes, Thin-Walled Structures 71(1), 134–146. https://doi.org/10.1016/j.tws.2013.05.003.

Minor, J., (1994). Windborne debris and the building envelope. Journal of Wind Engineering and Industrial Aerodynamics 53, 207–227. https://doi.org/10.1016/0167-6105(94)90027-2.

Meng, Q., Hao, H., Chen, W. (2016). Laboratory test and numerical study of structural insulated panel strengthened with glass fibre laminate against windborne debris impact. Construction and Building Materials 114, 434–446. https://doi.org/10.1016/j.conbuildmat.2016.03.190.

Mohotti, D., Ngo, T., Mendis, P., Raman, S.N., (2013). Polyurea coated composite aluminium plates subjected to high velocity projectile impact. Materials and Design 52, 1–16. https://doi.org/10.1016/j.matdes.2013.05.060.

Nedoushan, R.J., (2020). Improvement of energy absorption of expanded metal tubular structures under compressive loads, Thin-Walled Structures 157, 107058. https://doi.org/10.1016/j.tws.2020.107058.

Nouri, M.D., Hatami, H., Jahromi, A.G., (2014). Experimental and numerical investigation of expanded metal tube absorber under axial impact loading. Structural Engineering and Mechanics 54(6), 1245–1266. http://dx.doi.org/10.12989/sem.2015.54.6.1245.

Pathirana, M., Lam, N., Perera, S., Zhang, L., Ruan, D., Gad, E., (2017). Damage modelling of aluminium panels impacted by windborne debris. Journal of Wind Engineering and Industrial Aerodynamics 165, 1–12. https://doi.org/10.1016/j.jweia.2017.02.014.

Paule, B., Irissou, J. F., Saunier, G., (2006). Daylighting optimisation of the new factory of Turbomeca in Bordes, France. In Proceedings of the the 23rd Conference on Passive and Low Energy Architecture, Geneva, Switzerland (pp. 6–8).

Rambo-Roddenberry, M., Mtenga, P.V., Walsh, K.K., (2012). Missile impact resistance of a metal mesh roofing system. Journal of Architectural Engineering 18(3), 199–205. https://doi.org/10.1061/(ASCE)AE.1943-5568.0000079.

Rico-Martínez, J.M., Brzezicki, M., Ruiz-Mugica, C.G., Lech, J., (2020). Daylight transmittance through expanded metal shadings. Journal of Facade Design and Engineering, 8:85–114. https://doi.org/10.7480/jfde.2020.1.4698.

Saini, D., Shafei, B., (2020). Performance of structural insulated panels with metal skins subjected to windborne debris impact. Composites Part B Engineering 198, 108163. https://doi.org/10.1016/j.compositesb.2020.108163.

Smith, D., Graciano, C., Martínez, G., (2014a). Quasi-static axial compression of concentric expanded metal tubes. Thin-Walled Structures 84(11), 170–176. https://doi.org/10.1016/j.tws.2014.06.012.

Smith, D., Graciano, C., Martínez, G., Teixeira, P., (2014b). Axial crushing of flattened expanded metal tubes, Thin-Walled Structures 85(1), 42–49. https://doi.org/10.1016/j.tws.2014.08.001.

Smith, D. J., Graciano, C. A., Teixeira, P., Martínez, G., Pertuz, A., (2016). Energy absorption characteristics of coiled expanded metal tubes under axial compression. Latin American Journal of Solids and Structures, 13, 3145-3160. https://doi.org/10.1590/1679-78253242.

Smith, D., Graciano, C., Martínez, G., (2021). Expanded metal: A review of manufacturing, applications and structural performance. Thin-Walled Structures, 160(3), 107371. https://doi.org/10.1016/j.tws.2020.107371.

Stoner, M., Pang, W., (2019). Development of a windborne debris impact fragility curve for Cross-Laminated Timber using experimental testing. Journal of Wind Engineering and Industrial Aerodynamics 190, 143–150. https://doi.org/10.1016/j.jweia.2019.04.017.

Taghipoor, H., Noori, M.D., (2018). Experimental and numerical study on energy absorption of lattice-core sandwich beam. Steel and Composite Structures 27(2), 135–147. https://doi.org/10.12989/scs.2018.27.2.135.

Taghipoor, H., Nouri, M.D., (2020). Axial crushing and transverse bending responses of sandwich structures with lattice core. Journal of Sandwich Structures and Materials 22(3), 572–598. https://doi.org/10.1177/1099636218761321.

Taghipoor, H., Eyvazian, A., Kumar, A. P., Hamouda, A. M., Gobbi, M., (2020). Experimental and numerical study of lattice-core sandwich panels under low-speed impact. Materials Today: Proceedings. 27, 1487–1492. https://doi.org/10.1016/j.matpr.2020.03.001.

Teixeira, P., Martínez, G., Graciano, C., (2016). Shear response of expanded metal panels. Engineering Structures 106:261–272. https://doi.org/10.1016/j.engstruct.2015.10.034.

Tsay, Y. S., Yang, C. H., Yeh, C. Y., (2022). evaluation of expanded metal mesh applied on building facades with regard to daylight and energy consumption: A case study of an office building in Taiwan. Buildings, 12(8), 1187. https://doi.org/10.3390/buildings12081187

Wang, C., Wang, H., Shankar, K., Hazell, P. J., (2022). Dynamic failure behavior of steel wire mesh subjected to medium velocity impact: Experiments and simulations. International Journal of Mechanical Science, 216, 106991. https://doi.org/10.1016/j.ijmecsci.2021.106991

Wang, C., Wang, H., Shankar, K., Morozov, E. V., Hazell, P. J., (2021). On the mechanical behaviour of steel wire mesh subjected to low-velocity impact. Thin-Walled Structures, 159, 107281. https://doi.org/10.1016/j.tws.2020.107281.